

Research Article

In Situ 3D Bioprinting Living Photosynthetic Scaffolds for Autotrophic Wound Healing

Xiaocheng Wang,^{1,2,3} Chaoyu Yang,^{2,3} Yunru Yu,^{2,3,4} and Yuanjin Zhao^{1,2,3,4} 

¹Department of Rheumatology and Immunology, Institute of Translational Medicine, The Affiliated Drum Tower Hospital of Nanjing University Medical School, Nanjing 210008, China

²Oujiang Laboratory (Zhejiang Lab for Regenerative Medicine, Vision and Brain Health), Wenzhou, Zhejiang 325001, China

³Wenzhou Institute, University of Chinese Academy of Sciences, Wenzhou 325001, China

⁴State Key Laboratory of Bioelectronics, School of Biological Science and Medical Engineering, Southeast University, Nanjing 210096, China

Correspondence should be addressed to Yuanjin Zhao; yjzhao@seu.edu.cn

Received 20 January 2022; Accepted 21 February 2022; Published 20 March 2022

Copyright © 2022 Xiaocheng Wang et al. Exclusive Licensee Science and Technology Review Publishing House. Distributed under a Creative Commons Attribution License (CC BY 4.0).

Three-dimensional (3D) bioprinting has been extensively explored for tissue repair and regeneration, while the insufficient nutrient and oxygen availability in the printed constructs, as well as the lack of adaptive dimensions and shapes, compromises the overall therapeutic efficacy and limits their further application. Herein, inspired by the natural symbiotic relationship between salamanders and algae, we present novel living photosynthetic scaffolds by using an in situ microfluidic-assisted 3D bioprinting strategy for adapting irregular-shaped wounds and promoting their healing. As the oxygenic photosynthesis unicellular microalga (*Chlorella pyrenoidosa*) was incorporated during 3D printing, the generated scaffolds could produce sustainable oxygen under light illumination, which facilitated the cell proliferation, migration, and differentiation even in hypoxic conditions. Thus, when the living microalgae-laden scaffolds were directly printed into diabetic wounds, they could significantly accelerate the chronic wound closure by alleviating local hypoxia, increasing angiogenesis, and promoting extracellular matrix (ECM) synthesis. These results indicate that the in situ bioprinting of living photosynthetic microalgae offers an effective autotrophic biosystem for promoting wound healing, suggesting a promising therapeutic strategy for diverse tissue engineering applications.

1. Introduction

Cutaneous wounds occur for many reasons such as genetic disorders, mechanical trauma, surgical resection, infections, and other diseases [1–5]. Their optimal healing presents a great challenge due to the multifactorial biology and the specific variability of wounds (size, shape, depth, position, duration, patients with diabetic or ischemic diseases, etc.) [6–10]. Extensive and deep defects often necessitate the transplantation of autografts or allografts for wound closure, which may suffer from the shortage of donor tissues, infectious risk, and immunogenic rejection [11–13]. As an alternative and promising option, tissue engineering scaffolds have been elaborated for treating various wounds, especially for the large, deep, and chronic wounds [14–17]. Unfortunately, it

is often difficult to fabricate the scaffolds with custom sizes and dimensions, which could adequately cover the wounds with varying depth or topography [18]. In addition, the insufficient nutrient and oxygen availability, particularly in the central regions of the macroscale scaffolds, compromises the overall therapeutic efficacy and results in poor regenerative outcomes [19–21]. Although many oxygen-delivery stratagems through incorporating inorganic peroxides, liquid peroxides, or fluorocarbons into the scaffolds have been made to alleviate systemic hypoxia, promote angiogenesis, enhance collagen remodeling, and accelerate wound closure, these oxygen-generating systems typically provide oxygen for several days and cannot sustain sufficient oxygen over the entire healing process [22, 23]. Therefore, the development of an innovative scaffold with self-adaptive topography

and sustained oxygen supply throughout the healing process of different wounds is still highly anticipated.

In this paper, inspired by the natural symbiotic relationship between salamanders and algae [24], we present a novel living photosynthetic scaffold by using an in situ three-dimensional (3D) bioprinting strategy for autotrophic wound healing, as schemed in Figure 1. As a primitive autotrophic microorganism, microalga undergoes oxygenic photosynthesis to convert carbon dioxide and water to carbohydrates and oxygen under light illumination [25]. When in a long-term symbiotic relationship with spotted salamanders, the alive algae inside the salamander cells feed on the released waste materials and then photosynthesize to produce oxygen to the host cells [24]. Benefiting from the oxygen-releasing capacity, together with their abundant bioactive components and excellent biocompatibility, the photosynthetic microalgae have recently been incorporated into many functional systems for biomedical applications [20, 26–28]. Additionally, owing to the design flexibility and anatomical accuracy, 3D bioprinting technology has been widely employed for the fabrication of both living cell-laden and acellular biomimetic constructs in tissue engineering [29–34]. In particular, some attempts have been performed by in situ bioprinting of tissue constructs at defect sites, which enables accurate filling of irregular-shaped defects and concurrence of in vivo integration with native tissues [35–40]. Thus, it is conceivable that the in situ bioprinting of the photosynthetic microalgae into wound sites would provide a self-adaptive platform with an autotrophic oxygen supply for versatile wound healing.

Herein, we employed a microfluidic-assisted bioprinting strategy to directly deposit the living microalgae-laden hollow fibrous (MA-HF) scaffolds into the defect sites for promoting wound closure (Figure 1). Microfluidic technology manipulates single or multiple fluids in microscale channels in the range of tens to hundreds of microns [41–43]. The integration of microfluidic systems with conventional 3D printing platforms enables the precise control of the compositional and structural properties of tissue engineering scaffolds during the printing process [44, 45]. Thus, in this study, the microalgae-laden hollow fibers were firstly generated by rapidly polymerizing the microalgae-laden fluid from a coaxial capillary microfluidic chip and then printed into the 3D scaffolds conforming to the irregular-shaped wounds. Owing to the oxygenic photosynthesis of the embedded living microalgae (*Chlorella pyrenoidosa*, one of the most cultivated unicellular microalgae), the scaffolds could produce sustainable oxygen under light illumination, which facilitated the cell proliferation, migration, and differentiation even in hypoxic conditions. It was demonstrated that when the living microalgae-laden scaffolds were directly printed into the diabetic chronic wounds and exposed to light illumination, they could significantly accelerate the wound closure by alleviating local hypoxia, increasing angiogenesis, and promoting extracellular matrix (ECM) synthesis. These results indicated that such living photosynthetic scaffolds with autotrophic oxygen-supply capacity could be promising candidates for wound healing and various tissue engineering applications.

2. Results and Discussion

In the present study, the living microalgae-laden hollow fibrous (MA-HF) scaffolds were fabricated by a microfluidic-assisted bioprinting method (Figure 1). Firstly, a coaxial capillary microfluidic chip was custom-made by coaxially inserting a spindle capillary (orifice diameter: 100 μm) into a tapered injection capillary (orifice diameter: 450 μm , Figure S1). The gelatin inner fluid (5% w/v) containing various CaCl_2 contents (0–2% w/v) was pumped into the inner spindle capillary. The mixture fluid of alginate (2.5% w/v) and GelMA (5% w/v) biopolymers was pumped into the outer tapered capillary. The hollow fibers were generated by first ionic crosslinking between the Ca ions and alginate biopolymers and subsequent photopolymerization of GelMA components under UV irradiation. The channel diameter of the hollow fibers could be controlled from 150 to 350 μm by changing the CaCl_2 contents in the range of 0.2–2.0% and the inner/outer flow rate in the range of 0.2–2.0 (Figure S2). Comparatively, an increase in the CaCl_2 contents led to a decrease in channel diameter, while an increased flow ratio resulted in an increased channel diameter. When the CaCl_2 contents and flow ratio were fixed as 0.8% and 1.0, a typical hollow fiber with a straight channel was obtained, whose outer and inner diameters were approximately 375 μm and 300 μm , respectively (Figure S3). By introducing the green microalgae (*Chlorella pyrenoidosa*) into the biopolymer matrix, the living microalgae-laden hollow fibers were generated and appeared light green, different from the colorless acellular fibers (Figure S4).

Subsequently, the coaxial microfluidic chip was used to replace the original printing head in a programmable 3D printer. The microfluidic-spun microfibers could be stacked into a 3D scaffold layer by layer on a dry petri dish (Figure 2 (a)), when the flow rate of the fluids well matched the moving speed of the printing head. As shown in Figures 2(b)–2 (d), the in situ printed constructs could be picked up with tweezers and maintained their shapes in the air. Because the diffusion rate of Ca ions in biopolymer fluid was slower than the printing speed, the solidification of the microfiber was incomplete when the fibers were layer-stacked into a 3D construct, contributing to the good connections of the fibrous struts with straight channels (Figures 2(e)–2(h)). Additionally, the programmable in situ printing platform also enabled feasible control over the dimensions and shapes of the 3D scaffolds (e.g., triangle, cubic, and cylinder constructs in Figure S5), indicating the potential application of in situ printing of living microalgae-laden scaffolds for repairing irregular-shaped defects. The microstructure of the obtained microalgae-laden hollow fibrous (MA-HF) scaffolds was visualized under a scanning electron microscope (SEM, Figures 2(i)–2(l) and Figure S6). The strut surface of the MA-HF scaffold was rougher and more wrinkled, in contrast to the smooth and flat surface of the acellular hollow fibrous (HF) scaffold (Figure S7). The microalgae (a spherical shape of 2–5 μm , Figure S8) were wrapped in hydrogels, distributed randomly on the scaffold surface or embedded in the scaffold struts, confirming the

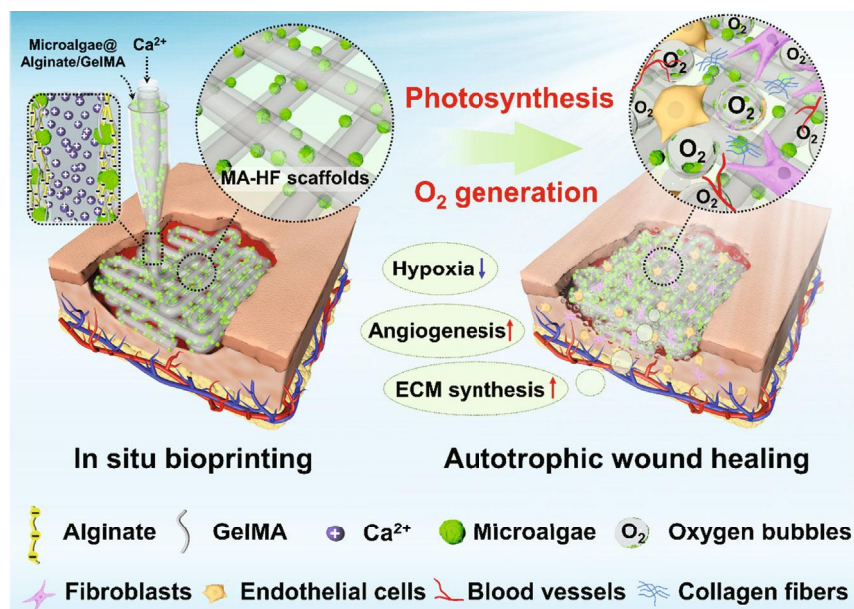


FIGURE 1: Illustration of in situ 3D bioprinting living photosynthetic scaffolds for autotrophic wound healing. The microalgae-laden hollow fibrous (MA-HF) scaffolds can be directly printed in freeform wounds due to the rapid crosslinking between the Ca ions and alginate-based pregels during a coaxial microfluidic printing process. After printing, the microalgae encapsulated in the MA-HF scaffolds serve as in situ autotrophic oxygen suppliers, which continuously generate oxygen under light illumination for enhanced wound healing by alleviating local hypoxia, accelerating angiogenesis, and promoting extracellular matrix (ECM) synthesis at wound sites.

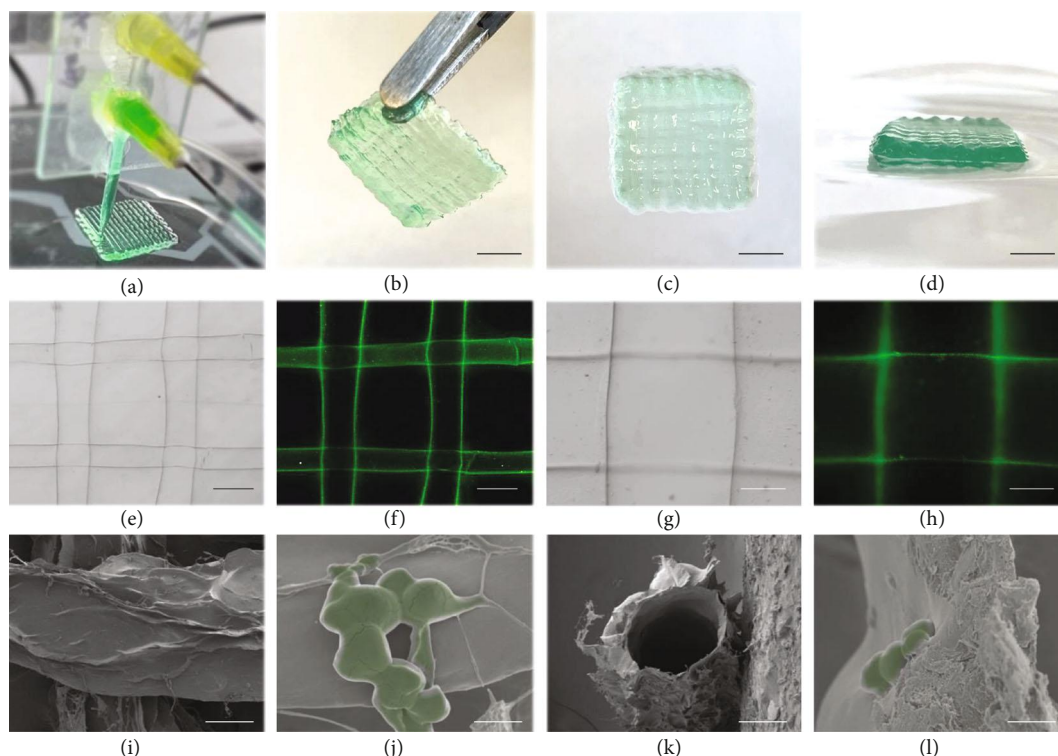


FIGURE 2: Characterization of MA-HF scaffolds. Photographs of (a) in situ microfluidic bioprinting process and (b–d) different views of the printed hollow fibrous scaffolds containing green dyes. (e–h) Optical and fluorescent micrographs of the hollow scaffolds with straight channels. Green: green fluorescent nanoparticles of 501/515 nm. (i, j) Top and (k, l) sectional views of the scanning electron microscopy (SEM) images of the freeze-dried MA-HF scaffolds at different magnifications. The microalgae encapsulated in the MA-HF scaffolds were shown in pseudogreen (j, l). The scale bars indicate 5 mm in (b–d), 300 μm in (e, f), 100 μm in (g, h, i, k), and 5 μm in (j, l), respectively.

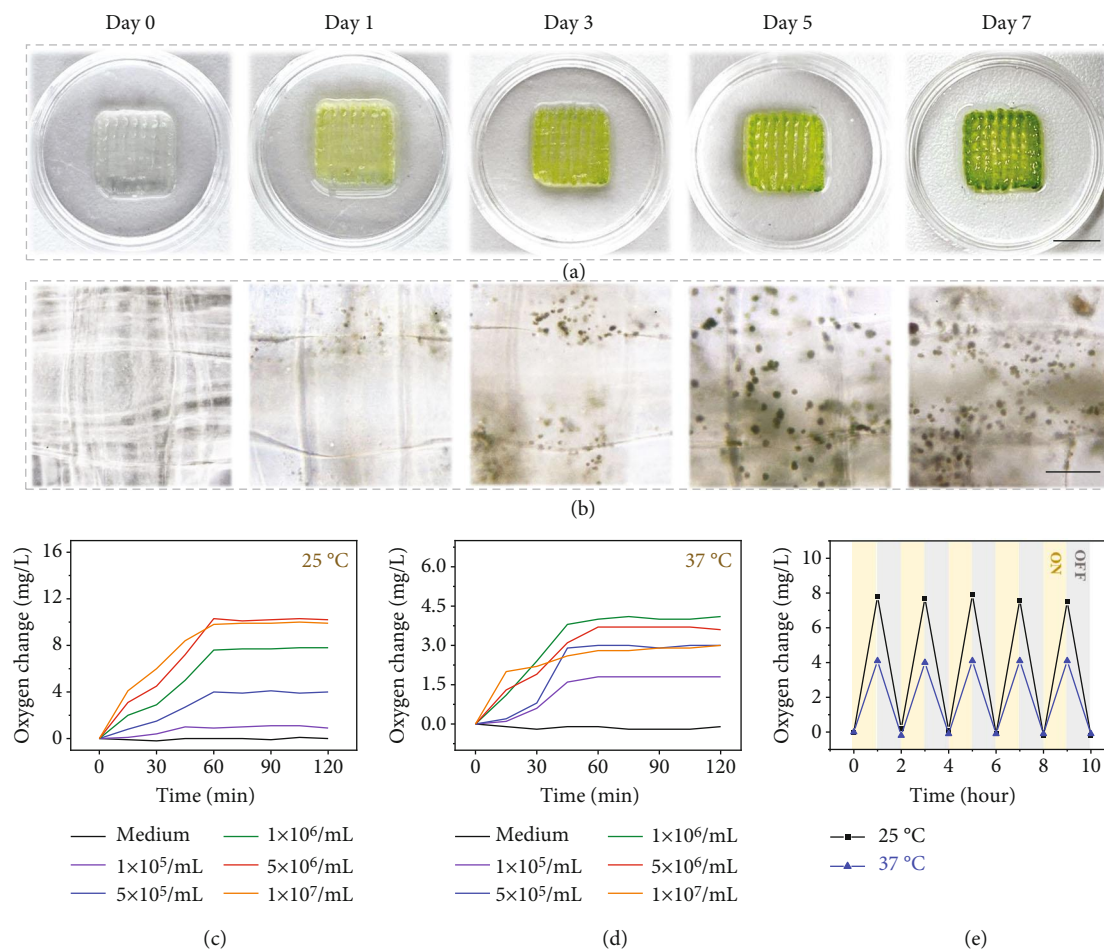


FIGURE 3: Photosynthetic oxygen-generating capability of MA-HF scaffolds. (a) Digital photographs and (b) bright-field microscopic images of MA-HF scaffolds cultivated for 7 days. (c, d) Quantification of oxygen changes in different MA-HF scaffolds with microalgae concentrations ranging from 10^5 to 10^7 /mL at (c) 25°C and (d) 37°C . (e) Comparison of oxygen releasing of MA-HF scaffolds under light (ON, yellow) and dark (OFF, gray) conditions at 25°C and 37°C . The scale bars indicate 1 cm in (a) and $150\ \mu\text{m}$ in (b).

successful incorporation of microalgae into the scaffold matrix. Altogether, the above results demonstrated the feasibility of the in situ bioprinting of living microalgae-laden scaffolds using the microfluidic-assisted bioprinting strategy.

Whereas the MA-HF scaffold was almost colorless after in situ printing, it gradually turned green when cultivated at 25°C under continuous light illumination (6000 lux) for 7 days (Figure 3(a)). Accordingly, the bright-field microscopic images revealed a distinct increase in the cell amounts over the culture period (Figure 3(b)), confirming that the microalgae survived from the in situ bioprinting process and maintained their proliferative ability within the scaffolds. To investigate the photosynthetic oxygenation activity of MA-HF scaffolds, the dissolved oxygen (DO) in the medium was monitored using an oxygen microsensor. A rapid increase in DO concentration could be detected in the first 60 min and then reached equilibrium under continuous light illumination, demonstrating the efficient oxygenation capacity of the photosynthetic microalgae encapsulated in MA-HF scaffolds (Figures 3(c) and 3(d)). Quantificationally, the increased DO concentration after 60 min illumination

was 0.9, 4.0, 7.8, 10.2, and 9.9 mg/L at 25°C with microalgae contents of 1×10^5 , 5×10^5 , 1×10^6 , 5×10^6 , and 1×10^7 cells/mL, respectively. The amount of oxygen released from MA-HF scaffolds was reduced when the microalgae content exceeded 5×10^6 , and a similar phenomenon also appeared when the microalgae content was above 1×10^6 at 37°C , indicating that the incorporation of too many microalgae in the scaffold may not be favorable for their growth and metabolism. The oxygen production at 37°C was inferior to that at 25°C , probably because the mammalian-cell culture condition might not be favorable for the microalgae cells. With consideration of further wound healing applications, we chose an optimal microalgae content of 1×10^6 cells/mL for subsequent studies. Notably, this oxygen-releasing behavior of MA-HF scaffolds was quite sensitive to the light/dark conditions, with an essentially constant increase in DO concentration of ~ 7.5 mg/L at 25°C and ~ 4.1 mg/L at 37°C , over five 60 min on/off cycles of light illumination (Figure 3(e)). Additionally, the photosynthetic oxygenation ability of MA-HF scaffolds was not significantly attenuated after storage at 4°C for 7 days (Figure S9). Collectively, all the above results confirmed that the encapsulated living microalgae in

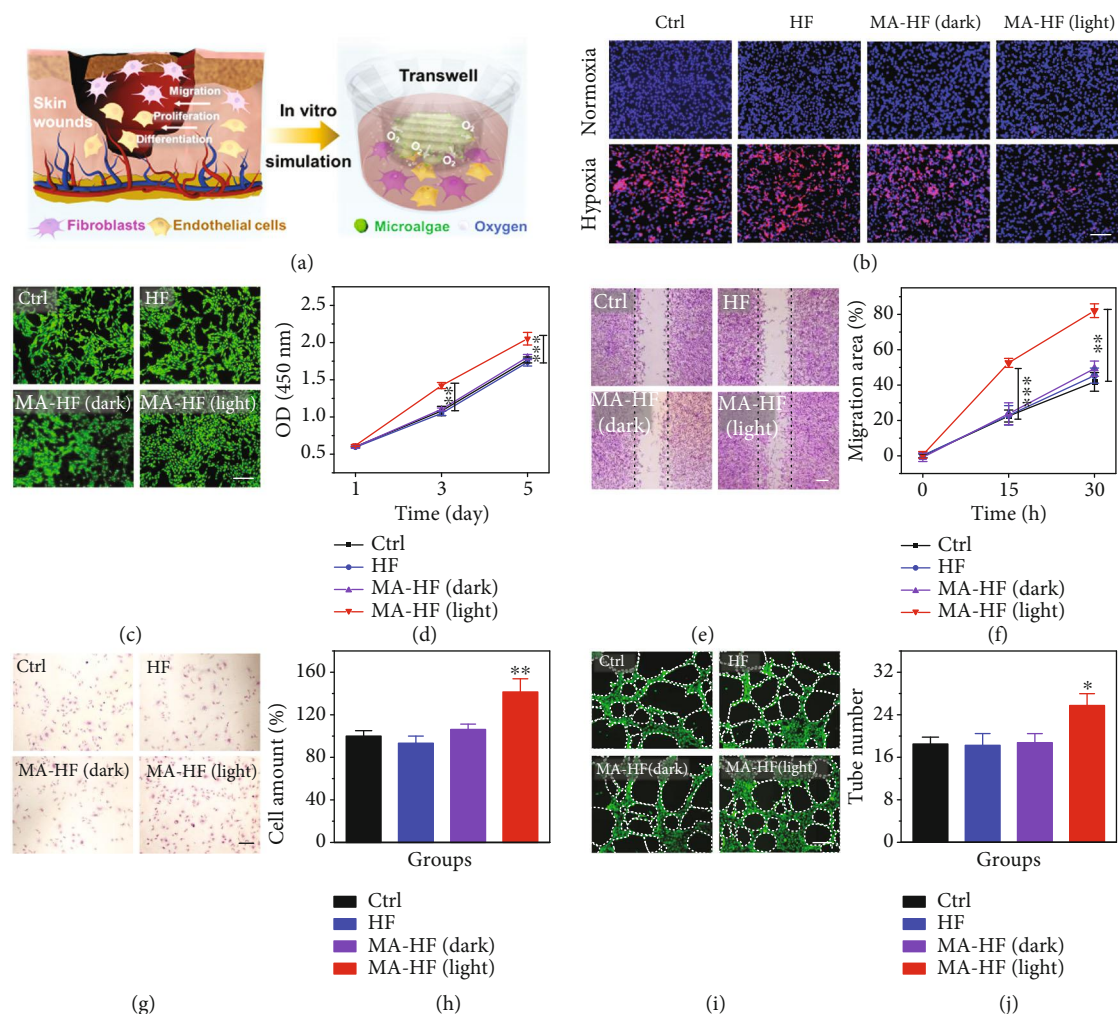


FIGURE 4: In vitro hypoxia alleviation by MA-HF scaffolds. (a) Schematic illustration of the in vivo skin wound healing process and in vitro experimental design for MA-HF scaffolds. (b) Fluorescent images of human skin fibroblasts (HSFs) incubated in normoxia or hypoxia (1% O_2) and double stained with hypoxia probe ($[Ru(dpp)_3]Cl_2$, red) and DAPI (blue). (c, d) Representative images and quantification of HSF cultured with HF or MA-HF scaffolds under hypoxic conditions (1% O_2) with or without light irradiation (6000 lux, 6 hours) for 5 days. (e, f) Representative images and quantification of in vitro scratch assay of HSFs. Dotted lines indicate initial scratch edges. (g, h) Representative images and quantitative analysis of transwell migration assay of human umbilical vein endothelial cells (HUVECs). (i, j) Representative images and quantification of tube formation of hypoxic HUVECs. Dotted circles indicate formed tubes. All scale bars indicate $200 \mu m$. $**p < 0.01$ and $***p < 0.001$ compared with control.

the MA-HF scaffolds endowed them with an effective and controllable oxygenation capacity by photosynthesis. The degradation behavior of MA-HF scaffolds was investigated after being soaked in phosphate-buffered saline (PBS, pH 7.4) for a certain period (Figure S10). It was found that the scaffolds lost their original shapes and mechanical strengths when immersed in PBS for 24h, and a mass loss of 85% was obtained after 5 days. Notably, the microalgae within the MA-HF scaffolds did not grow and gradually degraded in dark conditions. These results indicated that the MA-HF scaffolds are degradable in a physiological microenvironment, which is desirable for biomedical applications including tissue regeneration and wound healing.

Wound healing is an intricate and well-organized process that involves a sequence of events including the prolifer-

ation, migration, and differentiation of multiple cells such as fibroblasts and endothelial cells [5] (Figure 4(a)). Oxygen is required in every stage of the wound healing process, and hypoxia (i.e., a lack of oxygen supply) is the most common reason for impaired wound healing [22]. In our study, the MA-HF scaffolds are expected to release sufficient oxygen by photosynthesis to surrounding cells and protect them against hypoxia. Thus, the cellular hypoxic conditions were firstly simulated by culturing human skin fibroblasts (HSFs) and human umbilical vein endothelial cells (HUVECs) under low-oxygen conditions (1% oxygen). A common hypoxic indicator $[Ru(dpp)_3]Cl_2$ was utilized to detect intracellular hypoxia. It was found that the red fluorescence of HSFs incubated with MA-HF scaffolds in light was alleviated approximately to that in normoxia conditions, which is distinct from the large proportions of hypoxic cells in the HF,

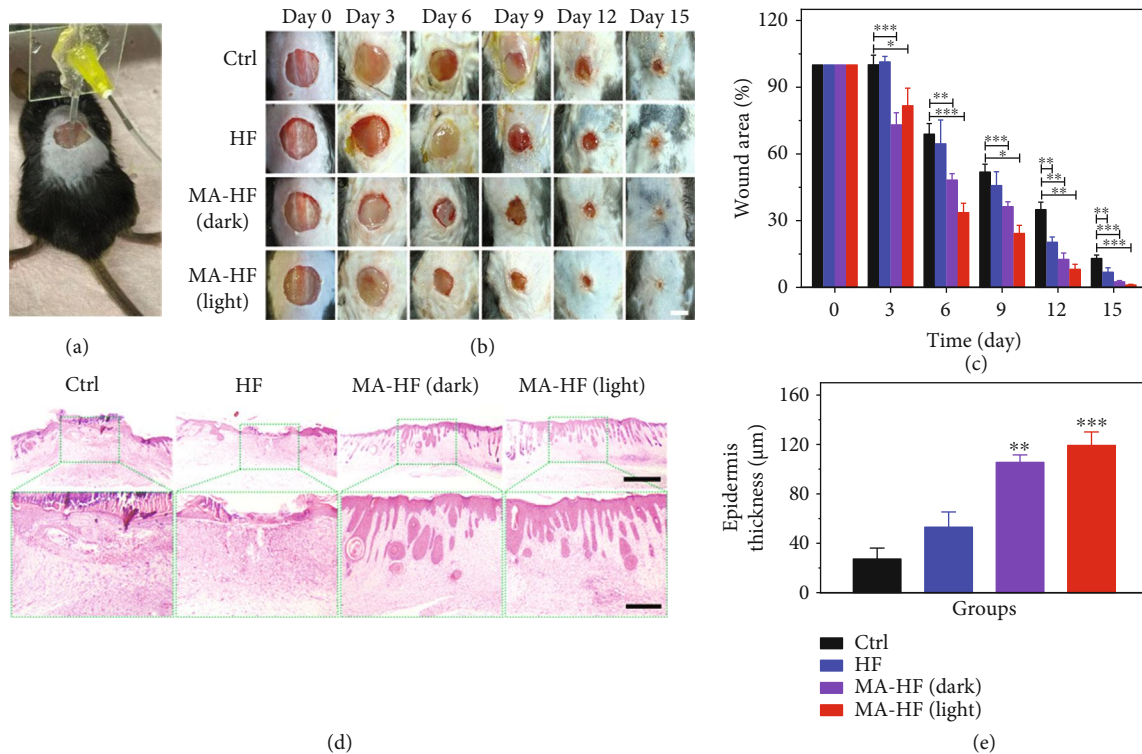


FIGURE 5: In situ bioprinting of MA-HF scaffolds for healing chronic wounds. (a) Representative photograph showing the MA-HF scaffold directly printed onto a murine diabetic wound via the microfluidic-driven printing strategy. (b) The wound healing process in different groups was tracked over 15 days. (c) Quantification of the in vivo wound closure at different time points. (d) Representative H&E staining images and (e) epidermis thickness of different groups on day 15. Dashed boxes indicate magnified regions. The scale bars indicate 5 mm in (b), 1 mm in (d, top), and 300 μm in (d, bottom). * $p < 0.05$, ** $p < 0.01$, and *** $p < 0.001$ compared with control.

MA-HF (dark), and control groups (Figure 4(b)). Benefiting from the hypoxia alleviated by the photosynthetic scaffolds, the cell proliferation of HSFs incubated with MA-HF scaffolds in light was significantly promoted as compared to that of the other groups (Figures 4(c) and 4(d)). To explore whether the photosynthetic scaffolds could promote cell migration in hypoxic conditions, a typical scratch assay was conducted. The results revealed that the wound closure of both HSFs and HUVECs was significantly accelerated in the MA-HF (light) groups in comparison to the other groups (Figures 4(e) and 4(f) and Figure S11). Furthermore, the enhanced cell mobility by MA-HF scaffolds in light was also confirmed by the transwell migration assay of hypoxic HUVECs (Figures 4(g) and 4(h)). To evaluate the angiogenic capability of photosynthetic MA-HF scaffolds, a Matrigel tube formation assay was performed and the results showed that more vessel-like tubes were observed after 6 hours in the MA-HF (light) groups than those in other groups (Figures 4(i) and 4(j)). Taken together, these results indicated the symbiotic relationship between mammalian cells and microalgae-laden scaffolds, which is consistent with previous studies [20, 28]. More importantly, our photosynthetic MA-HF scaffolds could effectively reverse the cellular hypoxia and improve the biological functions of mammalian cells under hypoxic conditions.

The in vivo wound healing potential of the photosynthetic MA-HF scaffolds was further investigated using a typ-

ical diabetic wound model regarding its chronic hypoxic features. Typically, the HF and MA-HF scaffolds were directly printed into the wounds on the dorsum of each mouse under anesthesia (Figure 5(a)). The healing process was tracked over 15 days, and the wounds healed faster with the treatment of MA-HF scaffolds as compared to the HF and control groups (Figure 5(b)). Quantitative analysis revealed that the relative wound area of the control, HF, MA-HF (dark), and MA-HF (light) groups on day 15 was $13.0 \pm 1.5\%$, $6.8 \pm 2.0\%$, $2.5 \pm 0.5\%$, and $1.1 \pm 0.3\%$, respectively (Figure 5(c)). Notably, the wound closure over the healing process did not show significant differences between the MA-HF (dark) and MA-HF (light) groups, indicating that the MA-HF scaffold exerted a stimulatory effect on wound healing even without light illumination. These results suggested that the degradable products of MA-HF scaffolds may be beneficial for wound healing, considering that the MA-HF scaffolds are degradable in a physiological microenvironment. Histological analysis was performed on day 15 with hematoxylin-eosin (H&E) staining and Masson's Trichrome staining. As shown in Figures 5(d) and 5(e), a thicker and more clear stratified epidermis layer with several appendages was formed in the two MA-HF groups, in dramatic contrast to the incomplete epidermis observed in the control and HF groups. Furthermore, the wounds treated with the MA-HF scaffold in light also showed the highest extents of collagen deposition ($51.6 \pm 3.0\%$), compared with

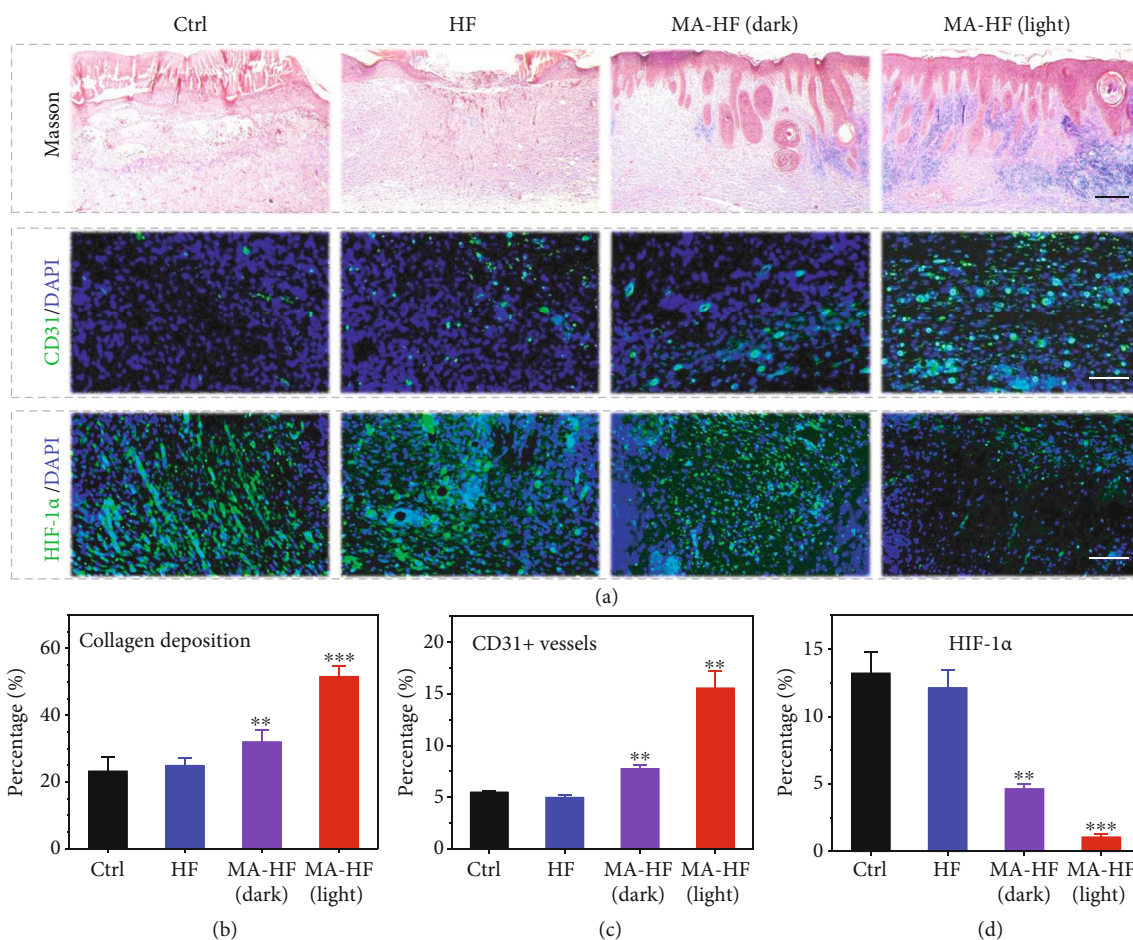


FIGURE 6: Accelerated collagen deposition, promoted angiogenesis, and alleviated tissue hypoxia by MA-HF scaffolds. (a) Masson's Trichrome staining (top) and immunofluorescence staining (CD31, middle; HIF-1 α , bottom) images of the regenerated skin tissues on day 15. Quantification of the (b) collagen deposition, (c) CD31-positive microvessel densities, and (d) HIF-1 α densities in different groups. All scale bars indicate 200 μ m in (a). ** p < 0.01 and *** p < 0.001 compared with control.

those in the control ($23.2 \pm 4.2\%$), HF ($24.9 \pm 2.2\%$), and MA-HF (dark, $32.0 \pm 3.4\%$) groups (Figures 6(a) and 6(b)), indicating the enhanced ECM reconstruction and tissue remodeling ability by the photosynthetic MA-HF scaffolds.

To explore the internal mechanism of the promoted wound closure by MA-HF scaffolds, immunohistochemical staining was performed using antibodies specific for CD31 (a typical marker of vascular endothelial cells) and HIF-1 α (hypoxia inducible factor α , the main indicator of tissue hypoxia, Figures 6(a), 6(c), and 6(d)). With the treatment of the MA-HF scaffolds in light, the density of CD31-positive microvessels was significantly increased ($15.6 \pm 1.6\%$), while the average microvessel densities were $5.5 \pm 0.1\%$, $5.0 \pm 0.2\%$, and $7.8 \pm 0.4\%$ in the control, HF, and MA-HF (dark) groups, respectively (Figure 6(c)). Conversely, the relative expression level of HIF-1 α in the MA-HF (light) group was $1.1 \pm 0.2\%$, which was considerably less than that in the control ($13.2 \pm 1.5\%$), HF ($12.1 \pm 1.2\%$), and MA-HF (dark, $4.6 \pm 0.4\%$) groups (Figure 6(d)). These findings suggested that the photosynthetic MA-HF scaffolds could effectively alleviate tissue hypoxia and promote angiogenesis in chronic wounds.

3. Conclusion

In summary, we have presented an in situ bioprinting strategy for fabricating the microalgae-laden hollow fibrous scaffolds with autotrophic oxygen-generating capability for adapting irregular-shaped wounds and promoting their healing. Owing to the oxygenic photosynthesis of the embedded living microalgae, the scaffolds could produce sustainable oxygen under light illumination, which facilitated cell proliferation, migration, and differentiation in low-oxygen culture conditions. Moreover, the living microalgae-laden scaffold could be directly printed into diabetic wounds and serve as an effective autotrophic biosystem to overcome the hypoxic microenvironment and accelerate the wound closure by increasing angiogenesis and promoting collagen synthesis. Therefore, our present work demonstrates the feasibility of in situ bioprinting of photosynthetic microalgae-laden scaffolds for autotrophic wound healing, which also provides an insightful therapeutic strategy for diverse tissue engineering applications. To adapt to irregular, curved, or deep wounds in complex biological environments, further optimization of microfluidic-assisted bioprinting is needed to

comprehensively demonstrate the efficacy. Our current printing system defined the scaffold geometry before printing. For real-time bioprinting, the intraoperative computerized imaging systems can be utilized to construct the real-time tomography of the tissue defects in the future. Moreover, the advances in microfluidic chips and functional materials with better bioprinting compatible properties will enable the microfluidic-assisted bioprinting to print more complicated 3D architectures into the curvilinear and deep tissue defects. To this end, we believe that our in situ bioprinting system will provide a facile and versatile strategy for repairing diverse defects in a rapid, safe, and automated manner.

4. Materials and Methods

4.1. Materials. Sodium alginate was purchased from Alfa Aesar. Methacrylate gelatin (GelMA), lithium phenyl-2,4,6-trimethylbenzoylphosphinate (LAP), and calcium chloride (CaCl_2) were bought from Shanghai Aladdin. Tris (4,7-diphenyl-1,10-phenanthroline) ruthenium (II) dichloride $\{[\text{Ru}(\text{dpp})_3]\text{Cl}_2\}$ was obtained from Shanghai Macklin. The microalgae (MA, *Chlorella pyrenoidosa*) and the specialized microalgae culture medium were purchased from Nanjing Health Biotech. Ultrapure water ($18.2 \text{ M}\Omega\text{-cm}^{-1}$, Millipore) was used throughout the experiments.

4.2. Microfluidic Spinning of Microalgae-Laden Hollow Fibers. The microalgae-laden hollow fibers (MA-HF) were prepared using a coaxial microfluidic chip assembled from a piece of glass slide and two cylindrical glass capillaries. In a typical experiment, to generate the hydrogel fibers with hollow channels, a capillary with a spindle tip (orifice diameter: $100 \mu\text{m}$) was coaxially inserted into a capillary with a tapered tip (orifice diameter: $450 \mu\text{m}$, Figure S1), which were then glued to a glass slide with transparent epoxy resin. The outer phase was pregel aqueous solution containing GelMA (5% w/v), sodium alginate (2.5% w/v), and LAP (0.1% v/v). The inner phase was gelatin solution (5% w/v) containing various CaCl_2 contents (0~2% w/v). Both the inner and outer liquids were injected into the microfluidic chip using programmed syringe pumps with defined flow rates and then collected in a clean petri dish. The hollow fibers were firstly generated by the ion crosslinking reaction between Ca^{2+} and alginate and subsequent photopolymerization of the GelMA component under ultraviolet (UV, 365 nm, 100 W) light irradiation for 5 min. A series of microalgae-laden hollow fibers with various concentrations could be fabricated by varying the MA contents in the pregel solutions (MA content: 1, 5, 10, 50, or 100×10^5 cells/mL).

4.3. In Situ Bioprinting of Microalgae-Laden Hollow Fibrous Scaffolds. Microalgae-laden hollow fibrous scaffolds (MA-HF scaffolds) were in situ printed in a dry petri dish through the microfluidic-assisted bioprinting strategy. The custom-made capillary microfluidic chip was used to replace the original 3D printer nozzle. The scaffold geometry (sizes and shapes) for printing was designed using 3ds max 2020 software. The extrusion rate of the microfibers from the

microfluidic chip should match the moving speed of 3D printing platform for a fluent printing process. Typically, both the inner and outer flow rates were set at 2 mL/h, and the moving speed of the 3D printer was set at 5 mm/s. During printing, the ion crosslinking of the alginate component in the outer flow phase was initially induced by the diffusion of Ca ions from the inner flow phase. After printing, the crosslinking of the GelMA component was achieved by UV irradiation (365 nm, 100 W, 5 min). All liquids and reagents used for subsequent biological experiments were sterilized by filtration through a sterile 0.22 mm filter or exposure to UV irradiation (254 nm) overnight.

4.4. Characterizations. Optical bright-field and fluorescent images of the hollow microfibers and scaffolds (containing green fluorescent nanoparticles of 501/515 nm) were observed by a stereomicroscope (Olympus BX51, Tokyo, Japan). The microstructure and morphology of the freeze-dried microalgae and microalgae-laden fibrous scaffolds were characterized with scanning electron microscopy (SEM, SU8010, Hitachi, Japan).

4.5. Dissolved Oxygen Release from the Microalgae-Laden Hollow Scaffolds. The photosynthetic oxygen production capacity of MA-HF scaffolds (MA concentration: 10^6 cells/mL; size: $15 \text{ mm} \times 15 \text{ mm} \times 2 \text{ mm}$) was examined under the illumination of a LED light bulb. In this study, the light intensity was set at 6000 lux, because the optimum light regimes for the growth of *Chlorella pyrenoidosa* are under the light intensity of 5000 to 8000 lux according to the manufacturer's instructions. The distance between the scaffolds and the LED light was 10 cm. The growth of the microalgae within the MA-HF scaffolds was photographed every two days at 25°C. The photoautotrophic oxygen release from MA-HF scaffolds was recorded in real time using an oxygen microsensor under the light illumination at 25°C and/or 37°C. To test the controllable oxygen consumption and production, the MA-HF scaffold was exposed to the LED light (light on) for 60 min, followed by incubation in dark conditions (light off) for another 60 min. The 60 min light on/off cycle was repeated for 10 h.

4.6. In Vitro Degradation Behavior of the Microalgae-Laden Hollow Scaffolds. The initial weights of MA-HF scaffolds (MA concentration: 10^6 cells/mL; size: $20 \text{ mm} \times 20 \text{ mm} \times 3 \text{ mm}$) were weighed after being soaked in 2% CaCl_2 for 24 h. The scaffold was immersed in 2 mL of phosphate-buffered saline (PBS) and kept in dark at 37°C for 8 days. The scaffolds were photographed every day and weighed after wiping out water on the scaffold surface. The relative weight loss was calculated as follows: relative weight loss (%) = $(W_0 - W_t)/W_0 \times 100$. Here, W_t represented the scaffold weights at certain time points and W_0 represented initial weights.

4.7. Cell Culture. Human skin fibroblasts (HSFs, ATCC) were cultured in Dulbecco's modified eagle medium (DMEM) containing 10% of fetal bovine serum and 1% of penicillin-streptomycin double antibiotics, while human umbilical vein endothelial cells (HUVECs, ScienCell) were

cultured in the specified endothelial cell medium (ECM) in 5% CO₂ at 37°C.

4.8. Intracellular Hypoxic Alleviation. The intracellular hypoxic alleviation effect of MA-HF scaffolds was evaluated using a hypoxia indicator {[Ru(dpp)₃]Cl₂} with red fluorescence, which could be quenched by oxygen. HSFs were incubated in a 24-well plate (10⁵ cells/well) under normoxia for 12 h. For hypoxic groups, the cells were cultured in the hypoxic microenvironment (1% O₂) and the transwell inserts (0.4 μm pore-sized filters) loaded with MA-HF scaffolds (1 × 10⁶ cells/mL) or HF scaffolds (Φ 5 mm × 2 mm) were gently placed into the 24-well plate. The MA-HF scaffolds in the MA-HF (light) groups were then illuminated by the LED light (6000 lux) for 6 h. After another 6 h in dark, the MA-HF scaffolds were removed and the cell medium was replaced with fresh DMEM containing hypoxia probes (8 μg/mL). The probe solution was discarded after 4 h incubation at 37°C. The cells were washed with fresh DMEM and fixed in paraformaldehyde (4%). 4',6-Diamidino-2-phenylindole (DAPI, blue) was used to stain the cell nuclei for observation.

4.9. Cell Proliferation Assay. HSFs were cultured in a 24-well plate (1 × 10⁴ cells/well) for overnight. Transwell inserts (0.4 μm pore-sized filters) containing MA-HF scaffolds (1 × 10⁶ cells/mL) or HF scaffolds (Φ 5 mm × 2 mm) were gently transformed into the plate. The MA-HF scaffolds in the MA-HF (light) groups were illuminated by the LED light (6000 lux) for 6 h every day. The cells were incubated in the hypoxic microenvironment (1% O₂) with the scaffolds for 5 days, and their proliferative status was examined by CCK-8 assay. Additionally, the cell viability of the HSFs was visualized with double staining of Calcein-AM and PI.

4.10. Scratch Wound Healing Assay. HSFs or HUVECs were seeded in a 24-well plate (1 × 10⁵ cells/well in the lower chamber) and cultured in the hypoxic microenvironment (1% O₂). After 12 h, a sterile p200 pipette tip was used to scratch the single-layer cells. The unattached cells were rinsed with PBS twice. Transwell inserts (0.4 μm pore-sized filters) containing MA-HF scaffolds (1 × 10⁶ cells/mL) or HF scaffolds (Φ 5 mm × 2 mm) were gently transformed into the plate (in the upper chamber). The MA-HF scaffolds in the MA-HF (light) groups were continuously exposed to the LED light (6000 lux). The cells in the lower chambers were photographed at appropriate time points. The relative migration area was defined as: relative migration area (%) = (1 - W/W₀) × 100%. W represented the wound area at certain time points and W₀ represented the wound area immediately after scratching, which were acquired using ImageJ software.

4.11. Transwell Migration Assay. HUVECs were cultured in the transwell inserts with 8 μm pore-sized filters (1 × 10⁴ cells/well in the upper chamber) and incubated in a 24-well plate containing MA-HF scaffolds (1 × 10⁶ cells/mL, Φ 10 mm × 1 mm) or HF scaffolds (Φ 10 mm × 1 mm in the lower chamber) in 1% oxygen for 24 h. The MA-HF scaffolds

in the MA-HF (light) groups were continuously exposed to the LED light (6000 lux). Cotton swabs were used to remove the cells on the upper surface of transwell inserts. Crystal violet solution (0.1%) was used to stain the migrated cells to the bottom side of the filters. The cells in purple were photographed by an inverted optical microscope (Nikon, Japan).

4.12. Tube Formation Assay. Matrigel matrix (BD, USA) was used to coat a 24-well plate (250 μL per well) before the cell seeding of HUVECs (5 × 10⁴ cells/well). The transwell inserts loaded with MA-HF scaffolds (1 × 10⁶ cells/mL) and HF scaffolds (Φ 5 mm × 2 mm) were gently placed into the 24-well plate and kept in 1% oxygen under the LED light illumination (6000 lux) for 6 h. The tube formation of HUVECs was observed using a fluorescence microscope (Zeiss) after Calcein-AM staining.

4.13. In Vivo Chronic Wound Closure in Diabetic Mice. The male C57BL/6 mice (20~25 g, 7~8 weeks) were provided by Beijing Vital River Laboratory Animal Technology Co., Ltd. All rats were treated strictly according to the Laboratory Animal Care and Use Guidelines. The experimental protocol was approved by the Animal Care and Use Committee of Wenzhou Medical University (Zhejiang, China). Streptozotocin- (STZ-) induced diabetic mouse model was established by intraperitoneal injection of STZ (50 mg/kg, dissolved in 0.1 M citrate buffer, pH~4.5) into the mice. Four weeks later, blood glucose from tail blood was measured and the diabetic mice with blood glucose levels over 20 mM were selected for further experiments. The mice were randomly grouped as follows (n = 8): (1) control group, (2) HF group, (3) MA-HF (dark) group, and (4) MA-HF (light) group. A full-thickness wound (Φ 10 mm) was created on the shaved dorsum of each mouse, which was rapidly covered by the in situ bioprinting of HF or MA-HF scaffolds (Φ 10 mm × 2 mm). During printing, the prologs were firstly polymerized by the ion crosslinking between the alginate component and Ca ions within 2 min. Immediately after printing, 1 min UV irradiation was performed to polymerize the GelMA component in the prologs. The scaffolds were then shielded with an opaque adhesive bandage. The MA-HF scaffolds in the MA-HF (light) groups were exposed to the LED light (6000 lux) for 2 hours every three days. The skin wound areas were recorded using a digital camera and calculated as: relative wound area (%) = W_t/W₀ × 100%. Here, W_t represented the wound area on day t (t = 0, 3, 6, 9, 12, and 15) and W₀ represented the wound area immediately after wounding, which were acquired using ImageJ software. All mice were sacrificed and sampled on day 15. For histological analysis, typical hematoxylin-eosin (H&E) staining and Masson's Trichrome staining were performed. Moreover, immunohistochemical analysis of CD31 and HIF-1α was employed to evaluate the vascularity and tissue hypoxia in the regenerated skin tissues. The tissue slices (thickness: 5 μm) were incubated with anti-CD31 or HIF-1α antibodies. The cell nuclei were stained with DAPI. Both the CD31-positive vessels (green), HIF-1α

protein (green), and nuclei (blue) were observed under a fluorescence microscope (Zeiss).

4.14. Statistical Analysis. Data are expressed as means \pm standard deviations ($n \geq 4$). All graphs were created from OriginPro 2020 software. The statistical significance between two groups was calculated using two-tailed unpaired Student's t -tests, with a p value < 0.05 considered significant ($*p < 0.05$, $**p < 0.01$, and $***p < 0.001$).

Data Availability

All data needed to evaluate the conclusions in the paper are present in the paper and/or the Supplementary Materials. Additional data related to this paper may be requested from the authors.

Conflicts of Interest

The authors declare that there is no conflict of interest regarding the publication of this article.

Authors' Contributions

Y.J.Z. conceived the idea and designed the experiment; X.C. W. conducted experiments and data analysis; C.Y.Y. and Y. R.Y. participated in data analysis and discussion; W.X.C. and Y.J.Z. wrote the manuscript.

Acknowledgments

This work was supported by the National Key Research and Development Program of China (2020YFA0908200), the National Natural Science Foundation of China (52073060 and 61927805), the Shenzhen Fundamental Research Program (JCYJ20190813152616459), and the China Postdoctoral Science Foundation funded project (2021M700141).

Supplementary Materials

Figure S1: the photographs and optical images of the coaxial capillary microfluidic device. Figure S2: the optical images of hollow fibers generated from the microfluidic device at varied CaCl_2 concentrations or the inner/outer flow rates. Figure S3: the optical and fluorescent micrographs of the hollow fibers. Figure S4: the digital photographs of the continuous pure hollow fibers and microalgae-loaded hollow fibers. Figure S5: the digital photographs of the printed scaffolds with different shapes and sizes. Figure S6: the SEM images of the microalgae incorporated into the MA-HF scaffolds. Figure S7: the SEM images of the freeze-dried HF scaffolds at different magnifications. Figure S8: the SEM images of the microalgae at different magnifications. Figure S9: the oxygen production of MA-HF scaffolds under light illumination for 7 days. Figure S10: the in vitro degradation behavior of MA-HF scaffolds. Figure S11: the in vitro scratch assay of HUVECs cultured with HF or MA-HF scaffolds. (*Supplementary Materials*)

References

- [1] O. J. Harrison, J. L. Linehan, H. Y. Shih et al., "Commensal-specific T cell plasticity promotes rapid tissue adaptation to injury," *Science*, vol. 363, no. 6422, article eaat6280, 2019.
- [2] T. Hirsch, T. Rothoef, N. Teig et al., "Regeneration of the entire human epidermis using transgenic stem cells," *Nature*, vol. 551, no. 7680, pp. 327–332, 2017.
- [3] C. Y. Chen, H. Yin, X. Chen et al., "Ångstrom-scale silver particle-embedded carbomer gel promotes wound healing by inhibiting bacterial colonization and inflammation," *Science Advances*, vol. 6, no. 43, article eaba0942, 2020.
- [4] Y. Liang, J. He, and B. Guo, "Functional hydrogels as wound dressing to enhance wound healing," *ACS Nano*, vol. 15, no. 8, pp. 12687–12722, 2021.
- [5] M. Rodrigues, N. Kosaric, C. A. Bonham, and G. C. Gurtner, "Wound healing: a cellular perspective," *Physiological Reviews*, vol. 99, no. 1, pp. 665–706, 2019.
- [6] S. Mascharak, H. E. desJardins-Park, M. F. Davitt et al., "Preventing Engrailed-1 activation in fibroblasts yields wound regeneration without scarring," *Science*, vol. 372, no. 6540, article eaba2374, 2021.
- [7] A. P. Veith, K. Henderson, A. Spencer, A. D. Sligar, and A. B. Baker, "Therapeutic strategies for enhancing angiogenesis in wound healing," *Advanced Drug Delivery Reviews*, vol. 146, pp. 97–125, 2019.
- [8] R. E. Jones, D. S. Foster, and M. T. Longaker, "Management of chronic wounds-2018," *The Journal of the American Medical Association*, vol. 320, no. 14, pp. 1481–1482, 2018.
- [9] Y. Yang, K. Huang, M. Wang et al., "Ubiquitination flow repressors: enhancing wound healing of infectious diabetic ulcers through stabilization of polyubiquitinated hypoxia-inducible factor-1 α by theranostic nitric oxide nanogenerators," *Advanced Materials*, vol. 33, no. 45, article e2103593, 2021.
- [10] G. Chen, Y. Yu, X. Wu et al., "Microfluidic electrospray niacin metal-organic frameworks encapsulated microcapsules for wound healing," *Research*, vol. 2019, article 6175398, 11 pages, 2019.
- [11] G. Fiakos, Z. Kuang, and E. Lo, "Improved skin regeneration with acellular fish skin grafts," *Engineered Regeneration*, vol. 1, pp. 95–101, 2020.
- [12] B. K. Sun, Z. Sipsashvili, and P. A. Khavari, "Advances in skin grafting and treatment of cutaneous wounds," *Science*, vol. 346, no. 6212, pp. 941–945, 2014.
- [13] Y. Dhar and Y. Han, "Current developments in biofilm treatments: wound and implant infections," *Engineered Regeneration*, vol. 1, no. 1, pp. 64–75, 2020.
- [14] L. Y. Daikuara, X. Chen, Z. Yue et al., "3D bioprinting constructs to facilitate skin regeneration," *Advanced Functional Materials*, vol. 32, no. 3, article 2105080, 2021.
- [15] Y. Yu, Q. Wang, C. Wang, and L. Shang, "Living materials for regenerative medicine," *Engineered Regeneration*, vol. 2, pp. 96–104, 2021.
- [16] C. Fuchs, L. Pham, Y. Wang, W. A. Farinelli, R. R. Anderson, and J. Tam, "MagneTEskin-reconstructing skin by magnetically induced assembly of autologous microtissue cores," *Science Advances*, vol. 7, no. 41, article eabj0864, 2021.
- [17] D. Chouhan, N. Dey, N. Bhardwaj, and B. B. Mandal, "Emerging and innovative approaches for wound healing and skin regeneration: current status and advances," *Biomaterials*, vol. 216, article 119267, 2019.

- [18] N. Hakimi, R. Cheng, L. Leng et al., "Handheld skin printer: in situ formation of planar biomaterials and tissues," *Lab on a Chip*, vol. 18, no. 10, pp. 1440–1451, 2018.
- [19] R. W. Barrs, J. Jia, S. E. Silver, M. Yost, and Y. Mei, "Biomaterials for bioprinting microvasculature," *Chemical Reviews*, vol. 120, no. 19, pp. 10887–10949, 2020.
- [20] S. Maharjan, J. Alva, C. Camara et al., "Symbiotic photosynthetic oxygenation within 3D-bioprinted vascularized tissues," *Matter*, vol. 4, no. 1, pp. 217–240, 2021.
- [21] G. Li, Q. Han, P. Lu et al., "Construction of dual-biofunctionalized chitosan/collagen scaffolds for simultaneous neovascularization and nerve regeneration," *Research*, vol. 2020, article 2603048, 18 pages, 2020.
- [22] Y. Guan, H. Niu, Z. Liu et al., "Sustained oxygenation accelerates diabetic wound healing by promoting epithelialization and angiogenesis and decreasing inflammation," *Science Advances*, vol. 7, no. 35, article eabj0153, 2021.
- [23] P. A. Shiekh, A. Singh, and A. Kumar, "Exosome laden oxygen releasing antioxidant and antibacterial cryogel wound dressing OxOBand alleviate diabetic and infectious wound healing," *Biomaterials*, vol. 249, article 120020, 2020.
- [24] R. Kerney, E. Kim, R. P. Hangarter, A. A. Heiss, C. D. Bishop, and B. K. Hall, "Intracellular invasion of green algae in a salamander host," *Proceedings of the National Academy of Sciences*, vol. 108, no. 16, pp. 6497–6502, 2011.
- [25] A. Lehmuskero, M. Skogen Chauton, and T. Boström, "Light and photosynthetic microalgae: a review of cellular- and molecular-scale optical processes," *Progress in Oceanography*, vol. 168, pp. 43–56, 2018.
- [26] L. Sun, L. Fan, F. Bian, G. Chen, Y. Wang, and Y. Zhao, "MXene-integrated microneedle patches with innate molecule encapsulation for wound healing," *Research*, vol. 2021, article 9838490, 9 pages, 2021.
- [27] Y. Qiao, F. Yang, T. Xie et al., "Engineered algae: a novel oxygen-generating system for effective treatment of hypoxic cancer," *Science Advances*, vol. 6, no. 21, article eaba5996, 2020.
- [28] H. Chen, Y. Cheng, J. Tian et al., "Dissolved oxygen from microalgae-gel patch promotes chronic wound healing in diabetes," *Science Advances*, vol. 6, no. 20, article eaba4311, 2020.
- [29] H. Ravanbakhsh, V. Karamzadeh, G. Bao, L. Mongeau, D. Juncker, and Y. S. Zhang, "Emerging technologies in multi-material bioprinting," *Advanced Materials*, vol. 33, no. 49, article e2104730, 2021.
- [30] X. Li, B. Liu, B. Pei et al., "Inkjet bioprinting of biomaterials," *Chemical Reviews*, vol. 120, no. 19, pp. 10793–10833, 2020.
- [31] S. Mishriki, S. Aithal, T. Gupta, R. P. Sahu, F. Geng, and I. K. Puri, "Fibroblasts accelerate formation and improve reproducibility of 3D cellular structures printed with magnetic assistance," *Research*, vol. 2020, article 3970530, 15 pages, 2020.
- [32] R. Levato, T. Jungst, R. G. Scheuring, T. Blunk, J. Groll, and J. Malda, "From shape to function: the next step in bioprinting," *Advanced Materials*, vol. 32, no. 12, article e1906423, 2020.
- [33] S. V. Murphy, P. De Coppi, and A. Atala, "Opportunities and challenges of translational 3D bioprinting," *Nature Biomedical Engineering*, vol. 4, no. 4, pp. 370–380, 2020.
- [34] S. Mishriki, A. R. Abdel Fattah, T. Kammann, R. P. Sahu, F. Geng, and I. K. Puri, "Rapid magnetic 3D printing of cellular structures with MCF-7 cell inks," *Research*, vol. 2019, article 9854593, 13 pages, 2019.
- [35] K. K. Moncal, H. Gudapati, K. P. Godzik et al., "Intra-operative bioprinting of hard, soft, and hard/soft composite tissues for craniomaxillofacial reconstruction," *Advanced Functional Materials*, vol. 31, no. 29, article 2010858, 2021.
- [36] C. Zhou, Y. Yang, J. Wang et al., "Ferromagnetic soft catheter robots for minimally invasive bioprinting," *Nature Communications*, vol. 12, no. 1, p. 5072, 2021.
- [37] H. Li, F. Cheng, D. P. Orgill, J. Yao, and Y. S. Zhang, "Handheld bioprinting strategies for in situ wound dressing," *Essays in Biochemistry*, vol. 65, no. 3, pp. 533–543, 2021.
- [38] Y. Chen, J. Zhang, X. Liu et al., "Noninvasive in vivo 3D bioprinting," *Science Advances*, vol. 6, no. 23, article eaba7406, 2020.
- [39] Y. Wu, D. J. Ravnic, and I. T. Ozbolat, "Intraoperative bioprinting: repairing tissues and organs in a surgical setting," *Trends in Biotechnology*, vol. 38, no. 6, pp. 594–605, 2020.
- [40] G. Ying, J. Manriquez, D. Wu et al., "An open-source handheld extruder loaded with pore-forming bioink for *in situ* wound dressing," *Materials Today Bio*, vol. 8, article 100074, 2020.
- [41] Y. Yu, L. Shang, J. Guo, J. Wang, and Y. Zhao, "Design of capillary microfluidics for spinning cell-laden microfibers," *Nature Protocols*, vol. 13, no. 11, pp. 2557–2579, 2018.
- [42] Y. Yu, J. Guo, L. Sun, X. Zhang, and Y. Zhao, "Microfluidic generation of microspheres with ionic liquid encapsulation for flexible electronics," *Research*, vol. 2019, article 6906275, 9 pages, 2019.
- [43] J. Guo, Y. Yu, D. Zhang, H. Zhang, and Y. Zhao, "Morphological hydrogel microfibers with MXene encapsulation for electronic skin," *Research*, vol. 2021, article 7065907, 2021.
- [44] H. Zhang, G. Chen, Y. Yu, J. Guo, Q. Tan, and Y. Zhao, "Microfluidic printing of slippery textiles for medical drainage around wounds," *Advanced Science*, vol. 7, no. 16, article 2000789, 2020.
- [45] X. Wang, Y. Yu, C. Yang et al., "Microfluidic 3D printing responsive scaffolds with biomimetic enrichment channels for bone regeneration," *Advanced Functional Materials*, vol. 31, no. 40, article 2105190, 2021.